




Article

Theoretical Investigation of Responsivity/NEP Trade-off in NIR Graphene/Semiconductor Schottky Photodetectors Operating at Room Temperature

Teresa Crisci ^{1,2} , Luigi Moretti ¹  and Maurizio Casalino ^{2,*} 

¹ Department of Mathematics and Physics, University of Campania “Luigi Vanvitelli”, Viale Abramo Lincoln, 5, 81100 Caserta, Italy; teresa.crisci@na.isasi.cnr.it (T.C.); luigi.moretti@unicampania.it (L.M.)

² Institute of Applied Science and Intelligent Systems “Eduardo Caianiello” (CNR), Via Pietro Castellino, 111, 80131 Naples, Italy

* Correspondence: maurizio.casalino@na.isasi.cnr.it; Tel.: +39-081-6132345

Abstract: In this work we theoretically investigate the responsivity/noise equivalent power (NEP) trade-off in graphene/semiconductor Schottky photodetectors (PDs) operating in the near-infrared regime and working at room temperature. Our analysis shows that the responsivity/NEP ratio is strongly dependent on the Schottky barrier height (SBH) of the junction, and we derive a closed analytical formula for maximizing it. In addition, we theoretically discuss how the SBH is related to the reverse voltage applied to the junction in order to show how these devices could be optimized in practice for different semiconductors. We found that graphene/n-silicon (Si) Schottky PDs could be optimized at 1550 nm, showing a responsivity and NEP of 133 mA/W and 500 fW/ $\sqrt{\text{Hz}}$, respectively, with a low reverse bias of only 0.66 V. Moreover, we show that graphene/n-germanium (Ge) Schottky PDs optimized in terms of responsivity/NEP ratio could be employed at 2000 nm with a responsivity and NEP of 233 mA/W and 31 pW/ $\sqrt{\text{Hz}}$, respectively. We believe that our insights are of great importance in the field of silicon photonics for the realization of Si-based PDs to be employed in power monitoring, lab-on-chip and environment monitoring applications.

Keywords: graphene; silicon; photodetectors; internal photoemission effect; near-infrared



Citation: Crisci, T.; Moretti, L.; Casalino, M. Theoretical Investigation of Responsivity/NEP Trade-off in NIR Graphene/Semiconductor Schottky Photodetectors Operating at Room Temperature. *Appl. Sci.* **2021**, *11*, 3398. <https://doi.org/10.3390/app11083398>

Academic Editor: Maria Ferrara

Received: 4 March 2021

Accepted: 8 April 2021

Published: 10 April 2021

Publisher's Note: MDPI stays neutral with regard to jurisdictional claims in published maps and institutional affiliations.



Copyright: © 2021 by the authors. Licensee MDPI, Basel, Switzerland. This article is an open access article distributed under the terms and conditions of the Creative Commons Attribution (CC BY) license (<https://creativecommons.org/licenses/by/4.0/>).

1. Introduction

Silicon (Si) Schottky photodetectors (PDs) have attracted the interest of the scientific community due to the possibility of making Si suitable for detecting infrared (IR) radiation, which is the range of wavelengths included in the spectrum where Si has a negligible optical absorption due to its bandgap of 1.12 eV (1.1 μm). Schottky Si PDs are metal/Si junctions whose detection mechanism is based on the internal photoemission effect (IPE), that is, the photo-excitation of charge carriers in the metal and their emission into Si over the Schottky barrier of the junction [1–3]. In other words, in Si Schottky PDs the metal and not the Si is the active material absorbing the incoming optical radiation. In this context, both palladium silicide (Pd_2Si) and platinum silicide (PtSi) Schottky PDs have been extensively investigated for the realization of infrared CCD image sensors. $\text{Pd}_2\text{Si}/\text{Si}$ Schottky PDs were developed for satellite applications showing the ability to detect a spectrum ranging from 1 to 2.5 μm when cooled to a temperature of 120 K [4,5]. On the other hand, PtSi/Si Schottky PDs were developed for operation at longer wavelengths ranging from 3 to 5 μm [6,7], although they require a lower temperature of 80 K. A focal plane array (FPA) constituted by an array of 512×512 PtSi/Si pixels was realized, demonstrating the first spectacular convergence between Si photonics and electronics [8]. Unfortunately, these devices can only work at cryogenic temperature. Indeed, the low Schottky barrier height (SBH) required to achieve an acceptable efficiency (0.21 eV for PtSi [7] and 0.34 eV for $\text{Pd}_2\text{Si}/\text{Si}$ [4]) is comes at the cost of PD noise (dark current), which must be reduced by lowering the working

temperature. PD noise affects the noise equivalent power (NEP), that is, the minimum detectable optical power, which has a huge impact on both the device sensitivity and the bit error rate (BER) of a communication link. Higher Schottky barriers make it possible to achieve low noise, but they unfortunately also lead to low efficiencies. This efficiency–noise trade-off is a peculiar characteristic of the Schottky PDs based on the IPE.

In 2006, for the first time, it was theoretically proposed to use Schottky PDs for the detection of near-IR (NIR) wavelengths at room temperature [9], taking advantage of the interference phenomena occurring inside a high-finesse Fabry–Pérot microcavity. The main idea was to work with metal/semiconductor junctions characterized by higher SBHs in order to reduce the dark current and then to recover the device efficiency by increasing the metal absorption through the multiple reflections of the optical radiation inside the microcavity. Later, many other strategies were pursued to enhance the efficiency of these devices; indeed, surface plasmon polaritons (SPPs) [10,11], Si nanoparticles (NPs) [12], metallic antennas [13], and gratings [14] were proposed and investigated. In any case, the measured responsivity was lower than 30 mA/W [12] and 5 mA/W [15] for waveguide and free-space Schottky PDs, respectively. More important, the efficiency–noise trade-off of these Schottky PDs has never been optimized in terms of SBH for achieving high efficiency and low noise at the same time. The low responsivity (i.e., the ratio between the photogenerated current and the incoming optical power) of the Schottky PDs based on metals is mainly due to the small emission probability of the photo-excited carriers from the metal to the Si, related to the momentum mismatch.

Recently, graphene/Si Schottky PDs have shown higher efficiencies with respect to the metallic counterpart and, even if the physical mechanism behind this enhancement is still under debate, it seems related to the increased emission probability due to the two-dimensionality of the material [16–18]. Although graphene is characterized by a low optical absorption (2.3%) many approaches based on resonant-cavity-enhanced (RCE) configurations [19,20], plasmonic structures [21], waveguiding structures [22], and quantum dots [23] have been proposed to overcome this drawback. At present, graphene/Si PDs [18,22,24] show superior performance to the corresponding metallic PDs, representing the most promising solution to realize low-cost Si PDs operating in the NIR regime. In addition, graphene offers a novel attractive possibility: the graphene Fermi level (i.e., the SBH with Si), can be simply modified by applying a bias to the junction, making it feasible to optimize the efficiency–noise trade-off.

In this work we theoretically investigated the responsivity/NEP trade-off in graphene/semiconductor Schottky PDs operating at NIR wavelengths and at room temperature. First, we used the results of the recent literature to derive a responsivity/NEP analytical equation that can be maximized with an appropriate choice of SBH. Then, we reviewed the SBH dependence on the bias applied to the graphene/semiconductor junctions to show how the responsivity/NEP ratio could be maximized in practice. Finally, we numerically calculated both the responsivity and the NEP of graphene/semiconductor PDs discussing their possible applications and highlighting the validity limits of the proposed optimization process. Even if this work was carried out with the aim of gaining greater insight into graphene/Si PDs, it is worth mentioning that we trace here a general methodology which can also be applied to different semiconductors, such as: germanium (Ge), gallium arsenide (GaAs), and aluminum gallium arsenide (AlGaAs).

2. Theoretical Background

IPE theory was first developed by Fowler in 1931, and it was focused on the injection of electrons from a metal into vacuum [25]. Several authors have extended Fowler's theory to the emission of carriers into semiconductors, conceiving the modified Fowler theory [26–28] and providing the following expression for the internal quantum efficiency (IQE) η_{int} of IPE-based PDs, defined as the number of charge carriers N_e produced per absorbed photons N_{ass} [26]:

$$\eta_{\text{int}} = \frac{N_e}{N_{\text{ass}}} = \frac{1}{8E_F} \cdot \frac{(hv - q\Phi_B)^2}{hv} \quad (1)$$

where E_F represents the Fermi level, $hv = hc/\lambda$ is the energy of the incident photon (λ is the wavelength and c the speed of light in a vacuum), q is the electron charge, and Φ_B is the potential barrier at the interface between the metal and the semiconductor. This expression is derived by taking into account the ratio of charge carriers having kinetic energy *normal* to the surface of the junction, necessary to overcome the potential barrier. This mechanism usually leads to poor efficiency (about 1%) [29,30]; however, it has been demonstrated that two-dimensional materials replacing metals in the Schottky junctions provide an IQE enhancement [18]. In particular, in single-layer graphene (SLG)/semiconductor junctions a still higher ratio of photon conversion in charge carriers is observed. Regarding this, Amirmazlaghani et al. [18] explain how this can be ascribed to the molecular structure of the graphene. Indeed, the π orbitals are normal to the interface with the semiconductor, and the charge carriers' momentum can be directed only towards the semiconductor or in the opposite direction, leading to an enhancement of the emission probability up to $\frac{1}{2}$. When SLG is used as active medium in an IPE-based PD, Equation (1) can no longer be applied due to the linearity of the dispersion relation near the Dirac point [31], different density of states, and probability of emission. However, the IQE of Schottky PDs based on SLG has been derived as [18]:

$$\eta_{\text{int}}^{\text{SLG}} = \frac{1}{2} \cdot \frac{(hv)^2 - (q\Phi_B)^2}{(hv)^2}. \quad (2)$$

The responsivity R is related to $\eta_{\text{int}}^{\text{SLG}}$ by the following relation:

$$R = \frac{I_{ph}}{P_{inc}} = S \cdot \frac{1}{hv} \cdot \eta_{\text{int}}^{\text{SLG}} = \frac{S}{2} \cdot \frac{(hv)^2 - (q\Phi_B)^2}{(hv)^3} \quad (3)$$

where I_{ph} is the photogenerated current, P_{inc} is the incident optical power, and S is the graphene optical absorbance. It is worth mentioning that in Equation (3) the charge carrier q is been considered in order to express the responsivity in A/W. Graphene has an optical absorption related to the universal fine-structure constant $\alpha = e^2/(\pi\epsilon_0\hbar c)$ [32] and independent of the frequency, $A_G = \pi\alpha \approx 2.3\%$. Here we focus our attention on devices that provide the complete absorption of the incident radiation such as long waveguides and resonant structures, thus we consider $S = 1$.

As the Schottky barrier Φ_B decreases, more electrons can pass into the semiconductor, giving rise to higher responsivities, as shown in Equation (2). Unfortunately, the dark current I_d of the junction also increases as Φ_B diminishes due to thermal effects [33]:

$$I_d = A_j A^* T^2 \cdot e^{-\frac{q\Phi_B}{kT}} \quad (4)$$

where A_j is the area of the Schottky junction, A^* is the Richardson constant, T is the absolute temperature and k is the Boltzmann constant. Furthermore, there is a component of noise intrinsic to the photodetection mechanism: due to the quantized nature of the light, the current is constituted by a succession of random impulses, which cause fluctuations of the measured current (shot noise). The quadratic mean value of the fluctuations linked to both photocurrent I_{ph} and dark current I_d is the following:

$$i_s^2(\Phi_B) = 2qB(I_d(\Phi_B) + I_{ph}(\Phi_B)) \quad (5)$$

where B is the device bandwidth. In addition to the shot noise, there is a thermal noise (Johnson noise) with quadratic mean value:

$$i_R^2 = \frac{4kTB}{R_L}, \quad (6)$$

where R_L is the load resistance of the PD. Since the two contributions of the noise current are statistically independent, the total noise i_n is given by their squared sum:

$$i_n = \sqrt{2qB(I_d(\Phi_B) + I_{ph}(\Phi_B)) + \frac{4kTB}{R_L}} \tag{7}$$

At low signal levels $I_{ph} \ll I_d$, the condition to make the thermal noise negligible compared to the shot noise in Equation (7) is:

$$I_d \gg 2V_{th}/R_L, \tag{8}$$

where the thermal voltage $V_{th} = kT/q$. At room temperature, Equation (8) mainly depends on both SBH and R_L . Of course, if the thermal noise dominates the shot noise, i_n does not depend on the SBH and the optimization procedure reported here can no longer be adopted. Compared to the absolute value of i_n , its magnitude compared to the generated signal I_{ph} , defined as the signal-to-noise ratio $SNR = I_{ph}/i_n$, is even more important.

In order to find the value of photogenerated current I_{ph} that brings $SNR = 1$, we can take advantage of the definition of the SNR and considering Equations (7) and (8), we obtain:

$$SNR = \frac{I_{ph}}{\sqrt{2qB(I_d(\Phi_B) + I_{ph}(\Phi_B))}} = 1. \tag{9}$$

The square of the previous equation gives a quadratic form in the unknown I_{ph} ; by solving it we find:

$$I_{ph} = qB \left(1 \pm \sqrt{1 + \frac{2I_d}{qB}} \right). \tag{10}$$

This expression makes it possible to obtain the minimum incident optical power P_{inc} necessary to get $SNR = 1$ for a PD characterized by a responsivity R . Since the NEP is defined as the incident optical power P_{inc} necessary to get $SNR = 1$ divided by the square root of the bandwidth ($NEP = P_{inc}/\sqrt{B}$), we numerically obtain NEP by considering $B = 1$ Hz in Equation (10) and dividing it by the responsivity R :

$$NEP = \frac{q \left(1 \pm \sqrt{1 + \frac{2I_d}{q}} \right)}{R} \tag{11}$$

which reduces to the very well-known formula:

$$NEP \approx \frac{\sqrt{2qI_d}}{R}, \tag{12}$$

where $2I_d/q$ is much larger than 1 in typical PDs. It is worth noting that in Equation (12) the sign of R follows the sign of I_{ph} , as is clear when looking at Equation (3).

Optimized PDs are characterized by high responsivity and low NEP. However, by looking at Equations (3) and (12) it is clear that by increasing the SBH, the NEP improves at the expense of the responsivity. On the other hand, an SBH decrease is beneficial in terms of responsivity but it degrades the NEP. Hence, we sought investigate the Schottky barrier Φ_B that maximizes the R to NEP ratio. Toward this aim we introduce the function $G(\Phi_B) = \sqrt{\frac{R}{NEP}}$ using Equations (2)–(4), and (12):

$$G(\Phi_B) = \sqrt{\frac{R}{NEP}} = \frac{R}{\sqrt{2qI_d}} = C \cdot \frac{(hv)^2 - (q\Phi_B)^2}{\sqrt{T}(hv)^3} \cdot e^{\frac{q\Phi_B}{4kT}} = C \cdot g(\Phi_B) \tag{13}$$

where $C = 1/(2\sqrt[4]{2qA_jA^*})$ depends on the geometry through the junction area A_j and on the semiconductor through the Richardson constant A^* . Figure 1a displays the behavior of $g(\Phi_B)$ at 300 K for three different wavelengths, 1.3 μm , 1.55 μm , and 2 μm , showing the presence of a peak. By calculating the first and second derivatives of $G(\Phi_B)$ we can find the value Φ_B^* of SBH corresponding to this peak:

$$\Phi_B^* = -4kT \left[1 - \sqrt{1 + \frac{(h\nu)^2}{16(kT)^2}} \right]. \tag{14}$$

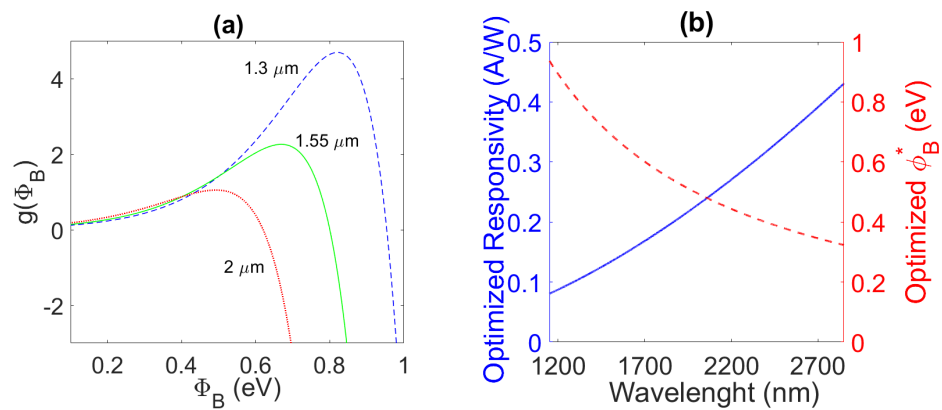


Figure 1. (a) Behavior of $g(\Phi_B)$ at 300 K for three wavelengths: 1.3 μm , 1.55 μm , and 2 μm ; (b) optimized responsivity R (blue solid line) and optimized Schottky barrier height (SBH) Φ_B^* (red dashed line) as a function of the wavelengths.

We define Φ_B^* as the optimized SBH because it is the value at which the R -to- NEP ratio is maximized. The dashed red line in Figure 1b shows the optimized Schottky barrier Φ_B^* as a function of the wavelength. This behavior can be explained by considering that when the wavelength is reduced the photon energy $h\nu$ increases by diminishing the responsivity R , as shown in Equation (3), requiring a reduction of the NEP to maintain the maximized R/NEP ratio. In turn, the NEP reduction can be achieved by an increase of the optimized Φ_B^* , which decreases the amount of charge carriers able to overcome the Schottky barrier due to thermal effects. Even if the Φ_B^* increment also produces a decrease in responsivity, it is important to recall that while the NEP is characterized by an exponential decay as a function of Φ_B^* ($NEP \sim e^{-\frac{\Phi_B^*}{2V_t}}$), the responsivity is characterized by a simple quadratic behaviour ($R \sim \Phi_B^{*2}$).

The substitution of Equation (14) in Equation (3) provides the responsivity when the ratio R/NEP is maximized (here we refer to it as the optimized responsivity), as shown by the blue solid line in Figure 1b. Note that this optimized responsivity depends only on the SBH of the junction. Figure 1b shows how the optimized responsivity is increased by increasing the wavelength owing to a drop in the optimized SBH Φ_B^* , providing values at room temperature of 0.10 A/W, 0.14 A/W, and 0.23 A/W at 1.3 μm , 1.55 μm , and 2 μm , respectively, as reported in Table 1. If higher responsivities are required, they can be achieved by lowering the SBH but at the expense of the SNR .

Table 1. Values of the Schottky barrier Φ_B^* optimizing the responsivity (R)/noise equivalent power (NEP) ratio at the three wavelengths of interest: 1.3 μm , 1.55 μm , and 2 μm at $T = 300$ K. The corresponding efficiency $\eta_{\text{int}}^{\text{SLG}}$ and responsivity R , calculated respectively through Equations (2), (3) and (14), are also shown. SLG is the acronym of single layer graphene.

λ (μm)	Φ_B^* (eV)	$\eta_{\text{int}}^{\text{SLG}}$	R (A/W)
1.3	0.86	0.10	0.10
1.55	0.7	0.11	0.14
2	0.52	0.14	0.23

3. Theoretical Results and Discussion

In this section we theoretically derive the SBH dependence on the bias applied to the junction in order to show how the graphene Schottky PDs based on different semiconductors could be optimized.

It is well-known that the SBH Φ_B of Schottky PDs can be determined by the two following equations (i.e., the Schottky–Mott relations) [33]:

$$q\Phi_B^{(n)}(V_R) = q\Phi_{\text{gr}}^0 - \Delta E_F(V_R) - q\chi_{\text{sm}} \quad (\text{n-type}) \quad (15)$$

$$q\Phi_B^{(p)}(V_R) = E_g - (q\Phi_{\text{gr}}^0 - \Delta E_F(V_R) - q\chi_{\text{sm}}) \quad (\text{p-type}) \quad (16)$$

where χ_{sm} and E_g are, respectively, the electron affinity and the bandgap of the semiconductor and $q\Phi_{\text{gr}}^0$ is the difference between the vacuum level E_0 and the Dirac point E_F^0 , while the graphene Fermi level is E_F (Figure 2). Therefore, $\Delta E_F = E_F - E_F^0$ can be expressed as [34]:

$$\Delta E_F = -\text{sgn}(n)\hbar v_F \sqrt{\pi|n|} \quad (17)$$

where $v_F = 1.1 \times 10^8$ cm/s is the Fermi velocity, \hbar is the reduced Planck constant, and n is the carrier density in graphene. The carrier density n not only depends on the graphene extrinsic doping n_0 (defined positive and negative for p-type and n-type graphene doping, respectively) but also on the thermal contact with the semiconductor. Indeed, when a p-doped graphene ($n_0 > 0$) is transferred onto the semiconductor, the space charge Q_{sm} in the depletion region induces an opposite charge $Q_{\text{gr}} = -Q_{\text{sm}}$ in the graphene layer. This creates additional charge carriers, modifying the carrier density, which becomes $n = n_0 + \frac{Q_{\text{gr}}}{q}$. The expression of the space charge Q_{sm} when the region is completely depleted is $Q_{\text{sm}} = \pm \sqrt{2\epsilon_{\text{sm}} N q V_{\text{bi}}}$, where ϵ_{sm} and N are the dielectric permittivity and the doping density of the semiconductor, respectively, while V_{bi} is the built-in potential. Moreover, by applying a reverse voltage, the charge per unit area in the graphene becomes $Q_{\text{gr}} = \mp \sqrt{2\epsilon_{\text{sm}} N q (V_{\text{bi}} + V_R)}$, providing a carrier density:

$$n = n_0 \mp \sqrt{\frac{2\epsilon_{\text{sm}}}{q} N (V_{\text{bi}} + V_R)} \quad (18)$$

where the signs minus and plus are for n- and p-type semiconductors, respectively. Equation (18) replaced into Equation (17) and then in Equation (15) or (16) gives the desired dependence between the SBH and the reverse bias V_R .

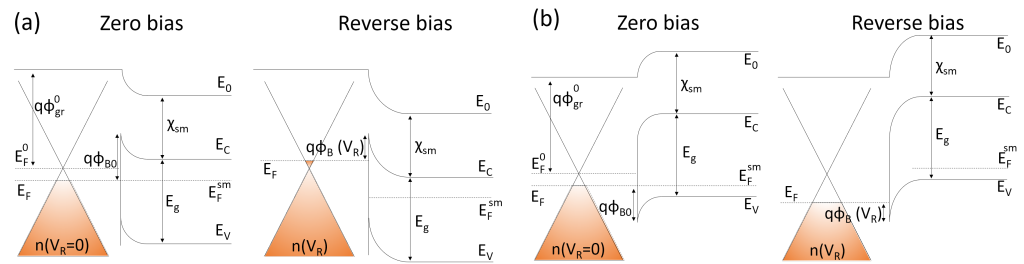


Figure 2. Band diagrams of (a) graphene/n-semiconductor and (b) graphene/p-semiconductor junctions at the thermal equilibrium and when a reverse bias V_R is applied. At the thermal equilibrium, graphene has an initial carrier density $n(V_R = 0)$. After a reverse bias this charge density becomes $n(V_R)$. E_0 represents the vacuum energy level while E_F^0 is the Dirac point. Φ_{gr}^0 , χ_{sm} , E_g , E_C , and E_V are respectively the intrinsic graphene work function, electron affinity, conduction band, bandgap, and valence band. E_F^{sm} is the Fermi energy level in the semiconductor and $q\Phi_{B0}$ the Schottky barrier at zero bias. The values of the Schottky barrier $q\Phi_B$ depend on the graphene Fermi energy level E_F that shifts when a voltage is applied.

In Table 2 we report the bandgap energy and the electron affinity for various semiconductors and the SBH at zero bias Φ_{B0} , calculated through Equation (15) or (16) when $V_R = 0$. The values of Φ_{B0} were evaluated by considering a graphene work function $\Phi_{gr}^0 = 4.6$ eV [35,36], a built-in potential $V_{bi} = 0.6$ V, an initial SLG extrinsic p-doping $n_0 = 10^{12}$ cm⁻², and a low doping of the semiconductors $N = 10^{16}$ cm⁻³.

Table 2. Bandgap E_g and electron affinity χ_{sm} of various semiconductors together with values of SBH when the Schottky junction is formed, calculated thanks to Equations (15)–(17) by taking into account an initial extrinsic p-doping $n_0 = 10^{12}$ cm⁻² of the single-layer graphene (SLG) and the thermal equilibrium contact with the substrate. For the calculations we considered low-doped semiconductors (i.e., $N = 10^{16}$ cm⁻³).

Semiconductor	E_g (eV)	χ_{sm} (eV)	$\Phi_{B0}^{(n)}$ (eV)	$\Phi_{B0}^{(p)}$ (eV)
Si	1.12	4.00	0.73	0.39
GaAs	1.43	4.07	0.66	0.77
Al _{0.3} Ga _{0.7} As	1.77	3.77	0.96	0.84
Ge	0.66	4.13	0.60	—

Figure 3a shows the intersections between these values of SBH Φ_{B0} for different semiconductors and the curve of the optimized $\Phi_B^*(\lambda)$ at room temperature (given by Equation (14)), suggesting the working wavelength to achieve the highest R/NEP ratio for each material. In the range of wavelengths where $\Phi_{B0} > \Phi_B^*(\lambda)$, the SBH can be lowered down to its optimal value as in Equation (14) by simply applying a specific reverse bias V_R to the junction.

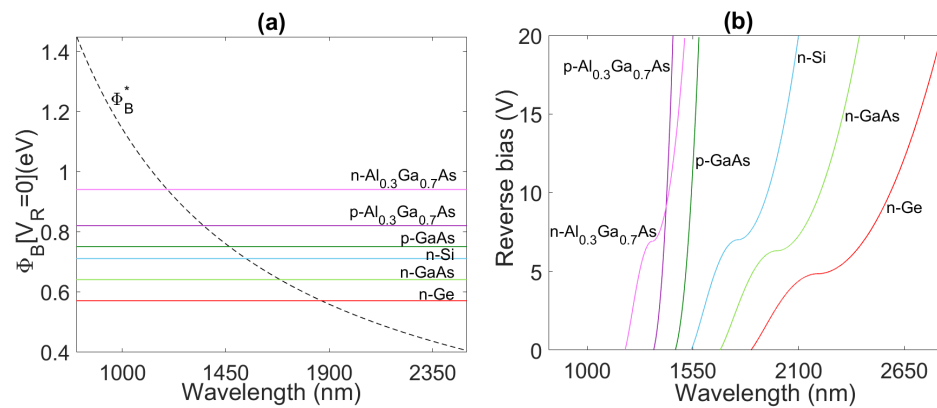


Figure 3. (a) Intersection between the curve $\Phi_B^*(\lambda)$ at 300 K and the values of SBH Φ_{B0} at the interface between graphene and several semiconductors in conditions of thermal contact (no voltage applied to the junction); (b) reverse voltage V_R to apply to the graphene/semiconductor junction as function of the wavelength for maximizing the signal-to-noise ratio (SNR) ($\Phi_B = \Phi_B^*$) for various semiconductors. The values of $\Phi_{B0} = \Phi_B(V_R = 0)$ were calculated through Equations (15)–(18) by considering an initial graphene p-doping of $n_0 = 10^{12} \text{ cm}^{-2}$ and a doping of $N = 10^{16} \text{ cm}^{-3}$ for all the semiconductors reported in Table 2.

By inverting Equation (18) and using Equation (17) and Equation (15) or (16) it is possible to calculate, for each wavelength and for each semiconductor, the values of the reverse voltage V_R such that $\Phi_B = \Phi_B^*$. We report this plot in Figure 3b by considering a maximum reverse bias of 20 V. It is interesting to observe that within this limit, graphene Schottky PDs based on p-Al_{0.3}Ga_{0.7}As and p-GaAs can be optimized only in a narrow window of the NIR spectrum, whereas n-Si can be optimized in a broader range, including at 1.55 μm where only a small reverse voltage $V_R = 0.66 \text{ V}$ for maximizing the R/NEP ratio is required. Indeed, at a reverse voltage of 0.66 V the $\Phi_{B0} = 0.73 \text{ eV}$ of the graphene/n-Si junction can be reduced to its optimum value of $\Phi_B^*(1.55 \mu\text{m}) = 0.71 \text{ eV}$. In contrast, p-GaAs requires a higher reverse voltage of 12 V to maximize R/NEP . Finally, n-Ge stands out among the analyzed semiconductors in view of the possibility to be employed over a region of the NIR spectrum above 2 μm . The range of wavelengths where R/NEP can be optimized for various semiconductors, by applying a reverse bias up to 20 V, is summarized in Table 3.

Table 3. Range of wavelengths in which the R/NEP ratio of the Schottky photodetectors (PDs) can be maximized by applying a reverse bias up to 20 V.

Semiconductor	λ_{\min} (nm)	λ_{\max} (nm)
<i>n - Si</i>	1541	2099
<i>p - GaAs</i>	1459	1582
<i>n - GaAs</i>	1692	2417
<i>p - Al_{0.3}Ga_{0.7}As</i>	1346	1447
<i>n - Al_{0.3}Ga_{0.7}As</i>	1197	1508
<i>n - Ge</i>	1852	2843

In Figure 4a,b we report the values of the quantities of interest in this work—the R/NEP ratio and the optimized NEP —for all the examined semiconductors by considering a graphene circular area with radius of 500 μm and a PD closed on a load resistance of 10 M Ω . We compute these optimized quantities through Equation (14) substituted into Equations (3) and (12). Recall that the results shown in Figure 4 are valid when the condition in Equation (8) is fulfilled. In order to verify it, we consider the dark current I_d one order of magnitude higher than $\frac{2V_{th}}{R_L}$ ($I_d = 10 \frac{2V_{th}}{R_L}$), and we calculate both optimized R/NEP and NEP by Equation (12). The solid black lines drawn in Figure 4a,b represent

the validity thresholds of our discussion: graphene Schottky PDs can be optimized in terms of R/NEP ratio at a given wavelength by means the use of semiconductors placed below and above the solid black lines drawn in Figure 4a,b, respectively. These thresholds depend on the load resistance R_L , the SBH Φ_B , and the graphene active area A_j , as is clearly shown by Equation (8). We discover that in the case analyzed here, only graphene/n-Si, graphene/n-Ge, and graphene/n-GaAs Schottky PDs can be suitable for this optimization procedure. Although Si is typically used for visible detection, analysis shows that graphene/n-Si Schottky PDs with a maximized R/NEP ratio could be adopted for detecting sub-bandgap NIR wavelengths with responsivity and NEP of 133 mA/W and 500 fW/ $\sqrt{\text{Hz}}$ at 1.55 μm , respectively. These devices provide low NEP , enabling their employment for power monitoring and lab-on-chip applications. Note that the predicted responsivity of graphene/n-Si PDs is higher than that reported for NIR Si PDs based on bulk-defect-mediated absorption. Indeed, taking advantage of mid-gap defects introduced into Si ring and disk resonators, Ackert et al. reported a responsivity of only 23 mA/W at -5 V [37] and 45 mA/W at -3 V [38] at 1560 nm, respectively. On the other hand, if the inter-band absorption of Ge is typically used for detecting the wavelength of 1.55 μm for telecommunications applications, graphene/n-Ge Schottky PDs could allow the detection of wavelengths longer than 1.55 μm , where the the Ge inter-band absorption suddenly decreases. Indeed, graphene/n-Ge Schottky PDs with optimized R/NEP ratio show a responsivity and NEP of 227 mA/W and 31 pW/ $\sqrt{\text{Hz}}$ at 2 μm , respectively, enabling their employment in environment monitoring applications. The predicted responsivity of graphene/n-Ge PDs is higher than that reported for NIR Ge PDs based on the introduction of tin (Sn) atoms in the Ge lattice. Indeed, with a substitutional Sn concentration of 6.5%, Ge-based PDs are able to absorb optical radiation at 2 μm but provide a limited responsivity of only 20 mA/W [39]. Note that NEP depends on many parameters, such as graphene's optical absorbance, the graphene area in contact with the semiconductor, and the temperature. Among these, particular attention should be paid to the temperature, which appears in the exponential argument of the dark current (Equation (4)), which in turn affects the NEP (Equation (12)). As an example, in a graphene/n-Si Schottky PD we evaluated this by increasing the temperature of 1 $^\circ\text{C}$ with respect to the room temperature, and an increase in optimized NEP below 5% could be achieved at any wavelength in the range of interest for this junction. As reported in Figure 4a,b, semiconductors such as n-Si, n-Ge, and n-GaAs can be exploited at room temperature for the realization of optimized graphene-based Schottky PDs in the spectral range from 1955 to 2080 nm with a responsivity from 219 to 245 mA/W (Figure 1b); however, while n-GaAs would be characterized by a lower NEP , n-Si and n-Ge would have the advantage of a better compatibility with CMOS technology.

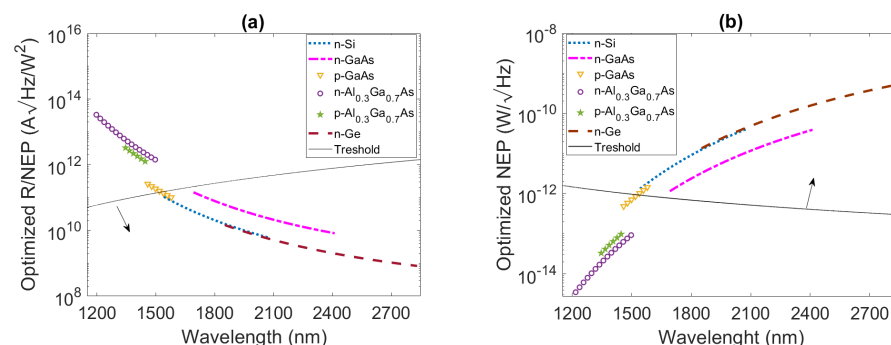


Figure 4. (a) The optimized R/NEP and (b) the optimized NEP of the Schottky graphene-based PDs for various semiconductors as function of the wavelength range individuated in Table 3. All figures were obtained at room temperature and by considering a graphene circular area in touch with the semiconductor with radius of 500 μm and a load resistance of 10 M Ω . The arrows indicate the validity regions of the proposed optimization procedure.

4. Conclusions

In this work we theoretically investigated the responsivity/NEP trade-off of NIR graphene/semiconductor Schottky PDs at room temperature. An analytical expression of the SBH able to maximize the R/NEP ratio was derived. Furthermore, we discussed how the optimized SBH can be tuned by applying a reverse voltage to the junction in order to establish the best operation conditions to achieve higher responsivity as well as lower noise for various semiconductors. Toward this aim we have accounted for the physics behind the emission of photo-excited charge carriers from graphene to Si, the theory of the graphene/semiconductor Schottky junctions, and the properties of graphene related to its two-dimensionality.

Remarkably, we found that CMOS-compatible materials such as Si and Ge could be exploited for the realization of optimized graphene Schottky PDs able to detect wavelengths beyond the limit imposed by their inter-band optical absorption. Indeed, graphene/n-Si Schottky PDs with maximized R/NEP ratio showed responsivity and NEP of 133 mA/W and 500 fW/ $\sqrt{\text{Hz}}$, respectively, at 1.55 μm by applying a reverse voltage of only 0.66 V. On the other hand, graphene/n-Ge Schottky PDs with maximized R/NEP ratio showed the potential to work at wavelengths longer than 1.55 μm , being for instance characterized by a responsivity and NEP of 227 mA/W and 31 pW/ $\sqrt{\text{Hz}}$ at 2 μm .

We believe that the insights reported in this work could be of paramount importance in silicon photonics for the realization of optimized PDs to be employed in power monitoring, lab-on-chip, and environment monitoring applications.

Author Contributions: Conceptualization, T.C. and M.C.; methodology, T.C., M.C., and L.M.; formal analysis, T.C. and M.C.; resources, L.M.; data curation, T.C., M.C. and L.M.; writing original draft preparation, T.C.; writing—review and editing, M.C. and L.M. All authors have read and agreed to the published version of the manuscript.

Funding: This research received no external funding.

Institutional Review Board Statement: Not applicable.

Informed Consent Statement: Not applicable.

Conflicts of Interest: The authors declare no conflict of interest.

References

1. Casalino, M. Internal photoemission theory: Comments and theoretical limitations on the performance of near-infrared silicon Schottky photodetectors. *IEEE J. Quantum Electron.* **2016**, *52*, 1–10. [[CrossRef](#)]
2. Scales, C.; Berini, P. Thin-film Schottky barrier photodetector models. *IEEE J. Quantum Electron.* **2010**, *46*, 633–643. [[CrossRef](#)]
3. Crisci, T.; Moretti, L.; Gioffrè, M.; Iodice, M.; Coppola, G.; Casalino, M. Integrated Er/Si Schottky Photodetectors on the end facet of optical waveguides. *J. Eur. Opt. Soc. Rapid Publ.* **2020**, *16*, 1–8. [[CrossRef](#)]
4. Elabd, H.; Villani, T.; Kosonocky, W. Palladium-silicide Schottky-barrier IR-CCD for SWIR applications at intermediate temperatures. *IEEE Electron Device Lett.* **1982**, *3*, 89–90. [[CrossRef](#)]
5. Elabd, H.; Villani, T.; Tower, J. High density Schottky barrier IRCCD sensors for SWIR applications at intermediate temperature. In Proceedings of the Society of Photo-Optical Instrumentation Engineers (SPIE) Conference, Arlington, TX, USA, November 1982; pp. 161–171.
6. Kosonocky, W.; Elabd, H.; Erhardt, H.; Shallcross, F.; Villani, T.; Meray, G.; Cantella, M.; Klein, J.; Roberts, N. 64×128 -Element high-performance PtSi IR-CCD imager sensor. In Proceedings of the International Electron Devices Meeting, Washington, DC, USA, 7–9 December 1981; p. 702. Available online: <https://ntrs.nasa.gov/citations/19830020268> (accessed on 9 April 2021).
7. Kosonocky, W.; Elabd, H.; Erhardt, H.; Shallcross, F.; Meray, G.; Villani, T.; Groppe, J.; Miller, R.; Frantz, V.; Cantella, M. Design And Performance of 64×128 Element PtSi Schottky-Barrier Infrared Charge-Coupled Device (IRCCD) Focal Plane Array. In Proceeding of the Society of Photo-Optical Instrumentation Engineers (SPIE), Infrared Sensor Technology, Arlington, USA, 28 December 1982; Volume 344, pp. 66–77.
8. Wang, W.L.; Winzenread, R.; Nguyen, B.; Murrin, J.J.; Trubiano, R.L. High fill factor 512×512 PtSi focal plane array. In *New Methods in Microscopy and Low Light Imaging*; International Society for Optics and Photonics: San Diego, CA, USA, 1989; Volume 1161, pp. 79–95.
9. Casalino, M.; Sirleto, L.; Moretti, L.; Della Corte, F.; Rendina, I. Design of a silicon resonant cavity enhanced photodetector based on the internal photoemission effect at 1.55 μm . *J. Opt. A Pure Appl. Opt.* **2006**, *8*, 909. [[CrossRef](#)]

10. Berini, P.; Olivieri, A.; Chen, C. Thin Au surface plasmon waveguide Schottky detectors on p-Si. *Nanotechnology* **2012**, *23*, 444011. [[CrossRef](#)]
11. Akbari, A.; Tait, R.N.; Berini, P. Surface plasmon waveguide Schottky detector. *Opt. Express* **2010**, *18*, 8505–8514. [[CrossRef](#)]
12. Zhu, S.; Chu, H.; Lo, G.; Bai, P.; Kwong, D. Waveguide-integrated near-infrared detector with self-assembled metal silicide nanoparticles embedded in a silicon pn junction. *Appl. Phys. Lett.* **2012**, *100*, 061109. [[CrossRef](#)]
13. Knight, M.W.; Sobhani, H.; Nordlander, P.; Halas, N.J. Photodetection with active optical antennas. *Science* **2011**, *332*, 702–704. [[CrossRef](#)]
14. Sobhani, A.; Knight, M.W.; Wang, Y.; Zheng, B.; King, N.S.; Brown, L.V.; Fang, Z.; Nordlander, P.; Halas, N.J. Narrowband photodetection in the near-infrared with a plasmon-induced hot electron device. *Nat. Commun.* **2013**, *4*, 1–6. [[CrossRef](#)]
15. Desiatov, B.; Goykhman, I.; Mazurski, N.; Shappir, J.; Khurgin, J.B.; Levy, U. Plasmonic enhanced silicon pyramids for internal photoemission Schottky detectors in the near-infrared regime. *Optica* **2015**, *2*, 335–338. [[CrossRef](#)]
16. Levy, U.; Grajower, M.; Goncalves, P.; Mortensen, N.A.; Khurgin, J.B. Plasmonic silicon Schottky photodetectors: The physics behind graphene enhanced internal photoemission. *APL Photonics* **2017**, *2*, 026103. [[CrossRef](#)]
17. Casalino, M.; Russo, R.; Russo, C.; Ciajolo, A.; Di Gennaro, E.; Iodice, M.; Coppola, G. Free-space schottky graphene/silicon photodetectors operating at 2 μm . *ACS Photonics* **2018**, *5*, 4577–4585. [[CrossRef](#)]
18. Amirmazlaghani, M.; Raissi, F.; Habibpour, O.; Vukusic, J.; Stake, J. Graphene-Si Schottky IR Detector. *IEEE J. Quantum Electron.* **2013**, *49*, 589–594. [[CrossRef](#)]
19. Casalino, M. Theoretical Investigation of Near-Infrared Fabry–Pérot Microcavity Graphene/Silicon Schottky Photodetectors Based on Double Silicon on Insulator Substrates. *Micromachines* **2020**, *11*, 708. [[CrossRef](#)] [[PubMed](#)]
20. Casalino, M. Design of resonant cavity-enhanced schottky Graphene/silicon photodetectors at 1550 nm. *J. Light. Technol.* **2018**, *36*, 1766–1774. [[CrossRef](#)]
21. Echtermeyer, T.; Britnell, L.; Jasnós, P.; Lombardo, A.; Gorbachev, R.; Grigorenko, A.; Geim, A.; Ferrari, A.C.; Novoselov, K. Strong plasmonic enhancement of photovoltage in graphene. *Nat. Commun.* **2011**, *2*, 1–5. [[CrossRef](#)] [[PubMed](#)]
22. Goykhman, I.; Sassi, U.; Desiatov, B.; Mazurski, N.; Milana, S.; De Fazio, D.; Eiden, A.; Khurgin, J.; Shappir, J.; Levy, U.; et al. On-chip integrated, silicon–graphene plasmonic Schottky photodetector with high responsivity and avalanche photogain. *Nano Lett.* **2016**, *16*, 3005–3013. [[CrossRef](#)]
23. Konstantatos, G.; Badioli, M.; Gaudreau, L.; Osmond, J.; Bernechea, M.; De Arquer, F.P.G.; Gatti, F.; Koppens, F.H. Hybrid graphene–quantum dot phototransistors with ultrahigh gain. *Nat. Nanotechnol.* **2012**, *7*, 363–368. [[CrossRef](#)] [[PubMed](#)]
24. Casalino, M.; Sassi, U.; Goykhman, I.; Eiden, A.; Lidorikis, E.; Milana, S.; De Fazio, D.; Tomarchio, F.; Iodice, M.; Coppola, G.; et al. Vertically illuminated, resonant cavity enhanced, graphene–silicon Schottky photodetectors. *ACS Nano* **2017**, *11*, 10955–10963. [[CrossRef](#)]
25. Fowler, R.H. The analysis of photoelectric sensitivity curves for clean metals at various temperatures. *Phys. Rev.* **1931**, *38*, 45. [[CrossRef](#)]
26. Elabd, H.; Kosonocky, W.F. PtSi Infrared Schottky-Barrier Detectors With Optical Cavity. *Review* **1982**, *43*, 569.
27. Cohen, J.; Vilms, J.; Archer, R.J. *Investigation of Semiconductor Schottky Barriers for Optical Detection and Cathodic Emission*; Technical Report; Hewlett-Packard Co.: Palo Alto, CA, USA, 1968.
28. Vickers, V.E. Model of Schottky Barrier Hot-Electron-Mode Photodetection. *Appl. Opt.* **1971**, *10*, 2190–2192. [[CrossRef](#)] [[PubMed](#)]
29. Raissi, F.; Far, M.M. Highly sensitive PtSi/porous Si Schottky detectors. *IEEE Sens. J.* **2002**, *2*, 476–481. [[CrossRef](#)]
30. Raissi, F. A possible explanation for high quantum efficiency of PtSi/porous Si Schottky detectors. *IEEE Trans. Electron Devices* **2003**, *50*, 1134–1137. [[CrossRef](#)]
31. Geim, A.; Novoselov, K. The rise of graphene. *Nat. Mater.* **2007**, *6*, 183–191. [[CrossRef](#)]
32. Nair, R.; Blake, P.; Grigorenko, A.; Novoselov, K.; Booth, T.; Stauber, T.; Peres, N.; Geim, A. Fine structure constant defines visual transparency of graphene. *Science* **2008**, *320*, 1308. [[CrossRef](#)] [[PubMed](#)]
33. Sze, S.M.; Ng, K.K. *Physics of Semiconductor Devices*; John Wiley & Sons: Hoboken, NJ, USA, 2006.
34. Neto, A.C.; Guinea, F.; Peres, N. KS Novoselov, and AK Geim. *Rev. Mod. Phys.* **2009**, *81*, 109.
35. Yu, Y.J.; Zhao, Y.; Ryu, S.; Brus, L.E.; Kim, K.S.; Kim, P. Tuning the graphene work function by electric field effect. *Nano Lett.* **2009**, *9*, 3430–3434. [[CrossRef](#)]
36. Takahashi, T.; Tokailin, H.; Sagawa, T. Angle-resolved ultraviolet photoelectron spectroscopy of the unoccupied band structure of graphite. *Phys. Rev. B* **1985**, *32*, 8317–8324. [[CrossRef](#)] [[PubMed](#)]
37. Ackert, J.; Fiorentino, M.; Logan, D.; Beausoleil, R.; Jessop, P.; Knights, A. Silicon-on-insulator microring resonator defect-based photodetector with 3.5-GHz bandwidth. *J. Nanophot.* **2011**, *5*, 0595071. [[CrossRef](#)]
38. Ackert, J.; Knights, A.; Fiorentino, M.; Beausoleil, R.; Jessop, P. Defect enhanced silicon-on-insulator microdisk photodetector. In Proceedings of the Optical Interconnects Conference, Santa Fe, NM, USA, 20–23 May 2012; Volume TuP10, pp. 76–77.
39. Xu, S.; Wang, W.; Huang, Y.C.; Dong, Y.; Masudy-Panah, S.; Wang, H.; Gong, X.; Yeo, Y.C. High-speed photo detection at two-micron- wavelength: Technology enablement by GeSn/Ge multiple-quantum-well photodiode on 300 mm Si substrate. *Opt. Express* **2019**, *27*, 5798. [[CrossRef](#)] [[PubMed](#)]